Chemo-Mechanical Modeling of Stress Evolution in All-Solid-State Lithium-Ion Batteries Using Synchrotron Transmission X-ray Microscopy Tomography

Hamed Fathiannasab[1], Likun Zhu[2], Zhongwei Chen[1]*

[1]Department of Chemical Engineering, University of Waterloo, Waterloo, ON N2L 3G1, Canada
[2]Department of Mechanical and Energy Engineering, Indiana University-Purdue University Indianapolis, Indianapolis, IN 46202, United States

---

Abstract

In this study, a chemo-mechanical modeling framework was developed by adopting a reconstructed three-dimensional morphology of all-solid-state lithium-ion battery (ASSB) composite electrodes, using a synchrotron transmission X-ray microscopy tomography system. The developed model aimed to elucidate the effects of the electrode microstructure, specifically solid electrolyte/active material (SE/AM) interface and void space, toward the lithiation-induced stress evolution. The results show that the peak stress points happen at the SE/AM interface, while void space can partially accommodate the AM swelling and alleviate the stress formation. Although applying higher pressing pressure during the electrode fabrication can improve the ion pathways, it adversely affects the stress formation and may cause crack propagation. The results reveal that SE stiffness has a key impact on stress formation and AM displacement. Although employing SE with a lower stiffness can attenuate the stress within the microstructure, it can exacerbate the anisotropic displacement of AM particles. In contrast, applying external pressing pressure can prevent anisotropic displacement of AM particles. The developed framework highlights the significance of microstructural design of ASSBs and provides invaluable insights.

Keywords

Chemo-mechanical modeling, all-solid-state lithium-ion battery, solid electrolyte/active material interface, solid electrolyte stiffness, anisotropic displacement

* Corresponding author: zhwchen@uwaterloo.ca

This is the author's version of the work published in final edited form as:

Fathiannasab, H., Zhu, L., & Chen, Z. (2021). Chemo-mechanical modeling of stress evolution in all-solid-state lithium-ion batteries using synchrotron transmission X-ray microscopy tomography. Journal of Power Sources, 483, 229028. https://doi.org/10.1016/j.jpowsour.2020.229028

1. Introduction

The widespread adoption of electric vehicles (EVs) highly relies on the development of high-performance electrochemical energy storage systems. In past years, conventional lithium-ion batteries (LIBs) are commonly used to power the EVs, although these batteries still face critical challenges such as the flammability of organic liquid electrolyte, limited operating temperature and voltage range, and limited capacity[1]. All-solid-state lithium-ion batteries (ASSBs) are a promising alternative to overcome the aforementioned drawbacks by employing an inflammable solid electrolyte (SE). They present less safety concerns and can facilitate high energy density cells by incorporating a lithium metal anode[2]. Despite the invaluable advantages of ASSBs, a multitude of factors need to be addressed. For instance, SEs, especially polymer solid-state electrolytes (SPEs), have poor ionic conductivity (10^{-6} $S.cm^{-1}$) and the interfacial incompatibility among inorganic ASSBs at the SE/active material (AM) interface[3] also hinders large scale employment of ASSBs.

The SE/AM interfacial contact tremendously impacts the performance of ASSBs, as in contrast to liquid electrolytes, the physical mismatch between the two solid phases creates void spaces at the interface. In ASSBs, the composite cathode is generally fabricated by mixing the SE, AM, and a conductive agent. The composite microstructure and morphological properties depend on the mixing conditions, such as the external pressing pressure and temperature [3], while poor interfacial contact limits the Li-ion transport pathways. Moreover, AM particle volume changes during lithiation/delithiation can lead to local stress buildup in the microstructure, fracture propagation, and capacity fading[4]. Therefore, microstructure design is highly critical in ASSBs in comparison to liquid electrolyte cells, where liquid electrolyte penetrates the porous electrode and the interfacial contact is not a remarkable issue. Most cathode AMs expand during lithiation;

although this volume change is negligible compared to that observed in alloy-based anode AMs, it is critical in ASSBs due to the solid/solid contact of the SE/AM interface. In other words, while liquid electrolyte cells can accommodate slight volume expansions of the cathode AM, for SE cells even minor volume changes could cause particle fracture and eventually pulverization[5]. Therefore, further investigation of the interfacial contact of ASSBs is crucial, since continuous expansion/contraction over the cycling of a cell can exacerbate the interfacial resistance and stress evolution.

The main sources of interfacial resistance at the SE/AM interface are the poor physical contact of the SE and AM [6], electrochemical instability of the SE/AM interface during cycling, and chemo-mechanical strain at the interface due to volume changes[7]. One of the effective approaches to improve the interfacial contact in ASSBs is to optimize external pressing pressure during the fabrication process[8]. The stress measurement techniques in ASSBs are generally categorized into the experimental methods: employing multi-beam optical stress sensor (MOSS) which correlate the stress/strain in a thin film to its curvature during cycling[9, 10], finite element method (FEM): developing an electrochemical-mechanical model to compute the stress/strain by solving transport equations in the microstructure[11], and analytical approach to calculate the stress evolution in ASSBs. It is worth noting that conducting *in situ* experiments on the SE/AM in ASSBs is difficult and time-consuming, whereas computational modeling can shed light on SE/AM morphological and electrochemical behavior and provide invaluable insights about ASSBs microstructural design[12].

There are a number of studies on the computational measurement of stress/strain in ASSBs available in the literature, which are mostly focused on 1D thin film[3, 13] or 2D planar geometries[11, 14, 15]. For instance, Bucci *et al.* developed the first quantitative analysis of the mechanical reliability of ASSBs by considering diffusion-induced volume changes. They reported that SEs with low stiffness are more likely to have micro-cracks due to their large deformation[11]. Moreover, Tian *et al.* developed a FEM-based electrochemical-mechanical model to evaluate stress in ASSBs. They reported that SE decomposition also causes volume change and consequently stress/strain formation in addition to diffusion-induced expansion[14]. They assumed an ideal physical contact at the SE/AM interface, although as discussed earlier, practical ASSBs do not have complete interfacial contact. Recently, Yu *et al.* studied the deformation and stresses in the ASSB electrode by employing a virtual polycrystalline microstructure. They investigated the sintering and lithiation-induced stress in the microstructure[16]. However, they assumed complete wettability of the SE while in realistic reconstructed microstructure of ASSBs, void space distribution has a remarkable effect on the electrochemical properties [12] and consequently on the lithiation-induced stress.

To accurately portray the effect of morphology on the stress/strain evolution in ASSBs, the 3D reconstructed microstructure can be a prominent solution. Among various ex-*situ* imaging techniques, computed tomography (CT) is commonly used for LIBs to reconstruct 3D morphology based on 2D CT images[17, 18]. Employing CT reconstructed morphology can shed light on the spatial distribution of physical and electrochemical parameters such as lithium concentration, current density, and overpotential within the SE and AM phase[12]. There are a few studies in the literature that have considered the 3D reconstructed microstructure of ASSBs[8, 19-22]. For instance, Ohashi *et al.* investigated the effect of stress distribution on the ion transport characteristics of the composite electrode using X-ray computed tomography[22]. They reported that for a composite electrode with sulfide solid electrolyte, the AM encounter larger stress at a high volume fraction of AM. Choi *et al.* investigated the physical properties of ASSBs' composite electrode using FIB-SEM imaging techniques and electrochemical analysis by using atom-probe tomography. They concluded that poor SE/AM interfacial contact causes remarkable lithium distribution within the electrode[19, 21]. Integrating a chemo-mechanical model for diffusion-induced stress modeling in ASSBs with 3D reconstructed morphology can highlight the stress/strain distribution at the SE/AM interface. The main advantage of a chemo-mechanical model based on the reconstructed morphology is quantifying the effects of physical and electrochemical properties on the ASSB's performance.

In this work, a chemo-mechanical model was implemented on 3D reconstructed ASSB morphologies fabricated under two different external pressing pressures for the first time. The primary goal is to understand the effect of the imperfect solid/solid interfacial contact of SE/AM on the stress/strain formation throughout charge-discharge cycling under a wide range of currents, as well as the effect of external pressing pressure on this phenomenon. The developed model has an electrochemical sub-model that includes diffusion and migration in the SE, diffusion in the AM, and charge transfer kinetics at the AM interface computed on a 3D reconstructed morphology. Moreover, the solid mechanics sub-model determines the diffusion induced stress/strain by employing a thermal-mass diffusion analogy. This paper is structured in the following format: first, the method of electrode preparation, electrode imaging with synchrotron transmission X-ray microscopy (TXM), and recronstruction of 3D morphology are presented. The Avizo™ software package was used to segment electrode images and build the 3D morphology. Then, the electrochemical and solid mechanics sub-models are discussed. The 3D modeling framework was implemented in Comsol Multiphysics 5.5. Finally, the simulation results are presented and discussed.

2. Experimental

2.1. Material synthesis and electrode fabrication

Ammonium dihydrogen phosphate ($(NH_4)_2H_2PO_4$), lithium carbonate (Li_2CO_3), aluminum oxide (Al_2O_3), and titanium dioxide (TiO_2) were employed to synthesize $Li_{1.3}Ti_{1.7}Al_{0.3}(PO_4)_3$ (LTAP). The solid mixture was ground and heated, ball milled for 6 hours, reheated for 2 hours, and then ball milled for 12 hours to obtain the final LTAP powder. The ASSB electrode was fabricated using $Li(Ni_{1/3}Mn_{1/3}Co_{1/3})O_2$ (NMC), Super-P carbon, and LTAP with a mass ratio of 47:6:47 (wt%). To investigate the effect of fabrication conditions on the electrode morphology, specifically SE/AM interface, the electrode was prepared under two different pressing pressures (700 psi and 1300 psi). The detailed synthesis method and fabrication steps are described in our previous work [23, 24]. The 1300 psi is the maximum applicable pressing pressure without damaging the assembled cell casing. Increasing the pressing pressure can increase the SE/AM interfacial contact and ion pathways, which could decrease the interfacial resistances and enhance cell performance.

2.2. TXM tomography

Electrode imaging was conducted at the beamline 32-ID-C of the Advanced Photon Source (APS) at Argonne National Laboratory employing TXM tomography. An 8 keV beam was utilized to capture 1000 images by rotating the sample for 180° with 2 s exposure time at each rotational step increment (0.25°). The voxel resolution was $58.2 \times 58.2 \times 58.2$ nm^3 and reconstructed morphology has $700 \times 700 \times 1000$ voxels. The segmentation steps using Avizo^{TM} were completely discussed before[8, 12]. The main challenge of ASSB electrode segmentation compared to LIB images is that the void space phase needs to be accurately determined since this phase blocks ion transport and the accuracy of the final results highly depends on it. The reconstructed morphologies of the electrode are presented in **Figure 1**. A median filter was applied to 2D images to reduce the noise of images. To increase the contrast between phases, a de-blur filter was used. Then, two thresholds were chosen manually. The grayscale gradient at the AM boundaries leads to the formation of a thin layer of SE, which is not realistic. Therefore, a dilation filter was used to replace this SE thin layer with the extension of AM particles. The superP phase cannot be distinguished from the TXM absorption contrast mode. Therefore, the SE domain is assumed to be the mixture of the super-P and solid electrolyte. In the developed model electron conduction is assumed to occur through the SE/AM interface. To separate the super-P phase in TXM images, the Zernike phase contrast mode, which is based on capturing the occurred contrast during the phase shift of the X-ray passing through the sample, should be considered. The Zernike mode can identify the super-P which is typically used in imaging of low-attenuation, low atomic number materials [1].

3. Modeling

In LIBs the volume change of the cathode AM is often neglected; however, in ASSBs the AM cathode particles are surrounded by the SE where a minor volume change could cause critical issues. During cycling, the lithiation/delithiation of AM particles leads to morphological changes within AM particles to accommodate Li-ions, whereas SE structural changes are negligible due to its intrinsic nature[7]. The developed model consists of the electrochemical sub-model to solve charge transfer kinetics at the AM interface, diffusion and migration of ions in the SE, and diffusion of ions in the AM. The equations have five unknown variables c_{Li}, c_{Li^+}, c_{n^-}, φ_s, and φ_{SE} which represent lithium concentration in the AM, lithium ion concentration in the SE, negative charge concentration in the SE, AM potential, and SE potential, respectively. The lithium concentration gradient within the AM is passed to the solid mechanics sub-model to determine the stress/strain evolution, which considers the SE/AM mechanical constraints in two different morphologies fabricated under different external pressing pressure.

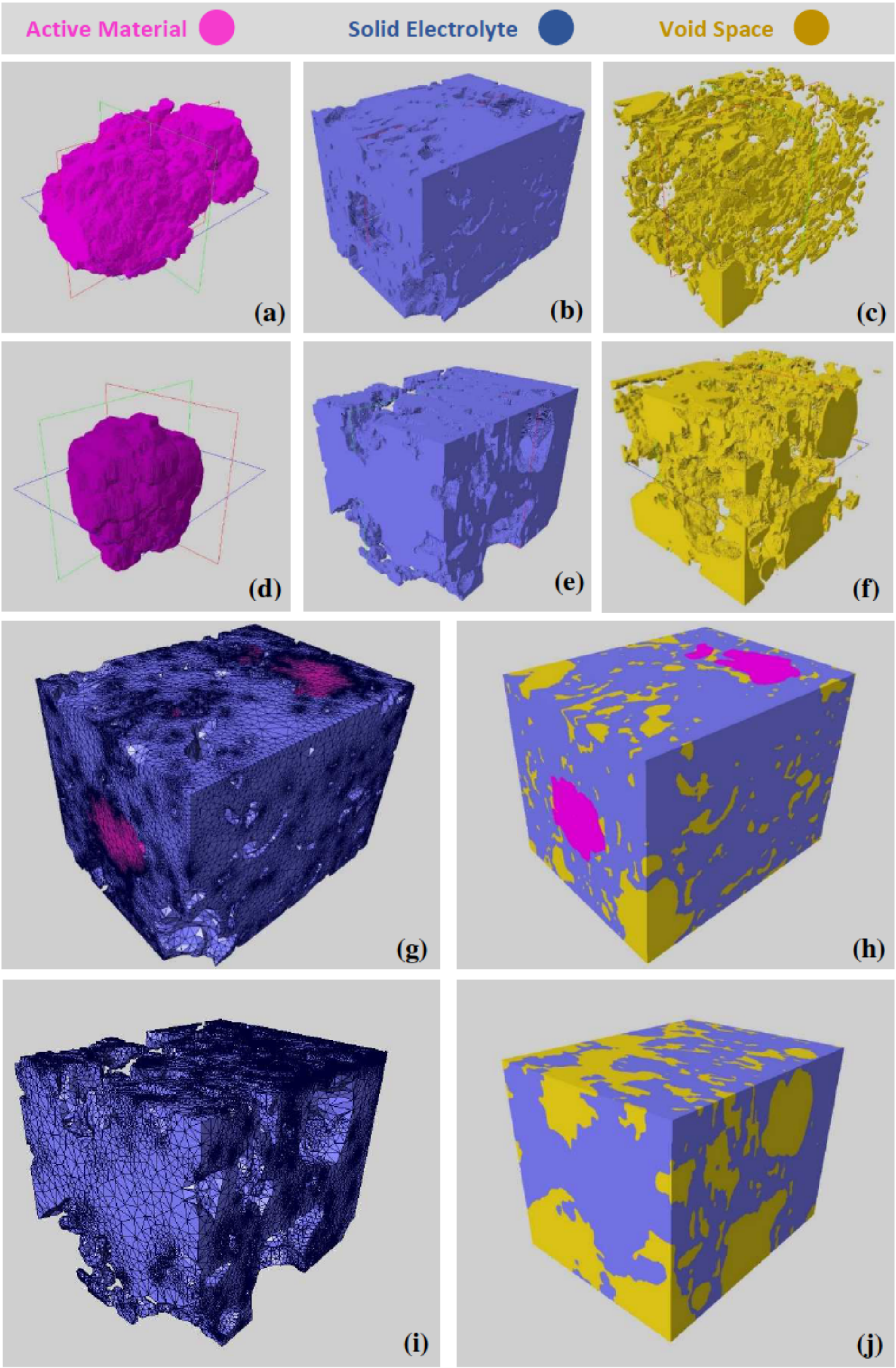

Figure 1 Reconstructed morphology of the electrode at two pressing pressures, (a-c) 1300 psi, (d-f) 700 Psi, (g) mesh and (h) reconstructed 3 phase electrode under 1300 psi pressing pressure, (i) mesh and (j) reconstructed 3 phase electrode under 700 psi pressing pressure.

3.1. Electrochemical sub-model

Although an inorganic SE behaves as a single-ion conductor[25]; it is widely common to simulate the SE as a binary electrolyte[26-28]. In a single ion-conducting electrolyte there is only one charged mobile species, Li$^+$, while in the binary electrolyte, the Li$^+$ and counterion are mobile. To implement a binary electrolyte methodology for SE simulation, electroneutrality $\sum z_k c_k = 0$ is assumed (k is either Li^+ or n^-). Therefore, at any time in the SE, $c_{Li^+} = c_{n^-}$. The overall reaction in SE is defined by:

$$r_d = k_d c_{Li^0} - k_r c_{Li^+} c_{n^-} \,, \tag{1}$$

where k_d is the dissociation rate of $Li \rightarrow Li^+ + n^-$, and k_r is the inverse reaction rate. At the equilibrium state, the mobile lithium defined by:

$$c_{Li^+}^{eq} = c_{n^-}^{eq} = \delta c_0 \,, \tag{2}$$

where $c_{Li^+}^{eq}$, $c_{n^-}^{eq}$, c_0, and δ are the lithium ion concentration at equilibrium, negative charge concentration at equilibrium, total lithium concentration, and fraction of mobile lithium in the SE, respectively. Nernst-Planck equation was implemented to simulate the lithium-ion transport behavior in the SE[12]:

$$\frac{\partial c_{Li^+}}{\partial t} + \nabla . -D_{Li^+} \nabla c_{Li^+} + \frac{z_{Li^+} F}{RT} D_{Li^+} c_{Li^+} \nabla \varphi_{SE} = r_d \,, \tag{3}$$

where z_{Li^+}, D_{Li^+}, F, φ_{SE} are the valence number, diffusion coefficient, Faraday's constant, and SE potential, respectively. Lithium diffusion within the AM phase was estimated by Fick's mass transport equation[18]:

$$\frac{\partial c_{Li}}{\partial t} = -\nabla . (-D_{Li} \nabla c_{Li}), \tag{4}$$

where c_{Li} and D_{Li} are the lithium concentration and diffusion coefficient of lithium in AM, respectively. Moreover, the rate of electrochemical reaction at the SE/AM interface is obtained using Butler-Volmer kinetics as:

$$i_{pos} = i_{0,pos}(e^{\frac{\alpha_{pos}F\eta}{RT}} - e^{-\frac{(1-\alpha_{pos})F\eta}{RT}}) \,, \tag{5}$$

$$i_{0,pos} = Fk_{pos}\left(\frac{(c_{Li,max} - c_{Li})c_{Li^+}}{(c_{Li,max} - c_{Li})c_{Li^+,0}}\right)^{\alpha_{pos}} \left(\frac{c_{Li} - c_{Li,min}}{c_{Li,max} - c_{Li,min}}\right)^{1-\alpha_{pos}} \,, \tag{6}$$

where i_{pos}, $i_{0,pos}$, k_{pos}, α_{pos}, $c_{Li,max}$ and $c_{Li,min}$ are the current density, exchange current density, apparent transfer coefficient, the reaction rate constant, and maximum and minimum of the lithium concentration in AM. The potential in the AM phase, φ_s, is described using Ohm's law in solids as follows:

$$i_{pos} = -\sigma_{pos}\nabla\varphi_s \,, \tag{7}$$

where σ_{pos} is the conductivity of solid AM. At all SE cube sides, $\nabla\varphi = 0 \; and \; \nabla c = 0$. The calculated lithium concentration in the AM and SE phases at each time step will be passed to the solid mechanics sub-model to calculate the diffusion induced stress formation.

3.2. Solid mechanics sub-model

In ASSBs, the SE/AM interface has a vital role since only lithium-ions can transport through this interface; however, the solid rigid surfaces of the SE and AM lead to a gap formation at the interface. Therefore, ASSBs cannot form a perfect SE/AM interface. At the microscopic level, diffusion-induced stress and strain exacerbate the contact problem[3]. To quantify the stress formation in the AM, SE, and SE/AM interface during cycling, a solid mechanics model was developed and coupled with the aforementioned electrochemical model. The deformation gradient is obtained by[29]:

$$F = (I + \nabla u), \tag{8}$$

where u is the displacement vector and I is the identity matrix. Lithium insertion leads to SE and AM volume expansion while the volume change depends on lithium concentration gradient Δc: [30]

$$\frac{V}{V_0} = \det(F_c) = 1 + \Omega \Delta c, \tag{9}$$

where V, V_0, and F_c are the current volume, initial volume, and lithium concentration induced deformation. The general definition of Ω is the partial molar volume change of host material after accommodating one mole of a guest atom. For lithium in NMC111, $\Omega = 3 \times 10^{-6}\ {m^3}/{mol}$ [4]. The lithiation induced deformation calculated by:

$$F_{c,ij} = \sqrt[3]{1 + \Omega \Delta c}\,\delta_{ij}, \tag{10}$$

where δ_{ij} is the Kronecker delta. To evaluate the stress formation, the Cauchy stress tensor σ can be derived by[31]:

$$\sigma = (\det(F))^{-1} F S F^T, \tag{11}$$

where S is the second Piola-Kirchhoff stress. In the electrode microstructure. To implement lithiation induced expansion, thermal-mass diffusion analogy was incorporated while temperature increment is replaced by a concentration difference. The strain is calculated by:

$$\varepsilon_{ij}^T = (\sqrt[3]{1 + \Omega \Delta c} - 1)\Delta c \delta_{ij} \tag{12}$$

In the second order stress tensor, there are three normal and three shear components. One of the effective ways to investigate volume change and distortion separately is employing hydrostatic stress and deviatoric stress, respectively. The hydrostatic stress can be obtained by calculating the average of the three normal stress components in the stress tensor:

$$\sigma_H = \frac{\sigma_{xx}+\sigma_{yy}+\sigma_{zz}}{3}, \tag{13}$$

where negative or positive σ_H represents compressive or tensile stress, respectively. The deviatoric stress σ' is equal to subtracting hydrostatic stress from the stress tensor.

$$\sigma' = \sigma - \sigma_H. \tag{14}$$

Moreover, von Mises stress is widely implemented to predict the yielding of materials under a complex loading condition. In other words, interpreting stress tensor is critical since it has six independent components; however, employing the von Mises criterion, which has a scalar value, analyzing, and comparison of the stress field in materials becomes straightforward. The von Mises stress can be calculated by:

$$\sigma_v = \sqrt{\frac{(\sigma_{xx}-\sigma_{yy})^2+(\sigma_{yy}-\sigma_{zz})^2+(\sigma_{xx}-\sigma_{zz})^2+6(\sigma_{xy}^2+\sigma_{yz}^2+\sigma_{zx}^2)}{2}}. \tag{15}$$

The boundary condition at the SE/AM interface is assumed to be a flexible attachment. The modeling methodology and all boundary conditions are illustrated in **Figure 2** and model parameters are presented in **Table 1**.

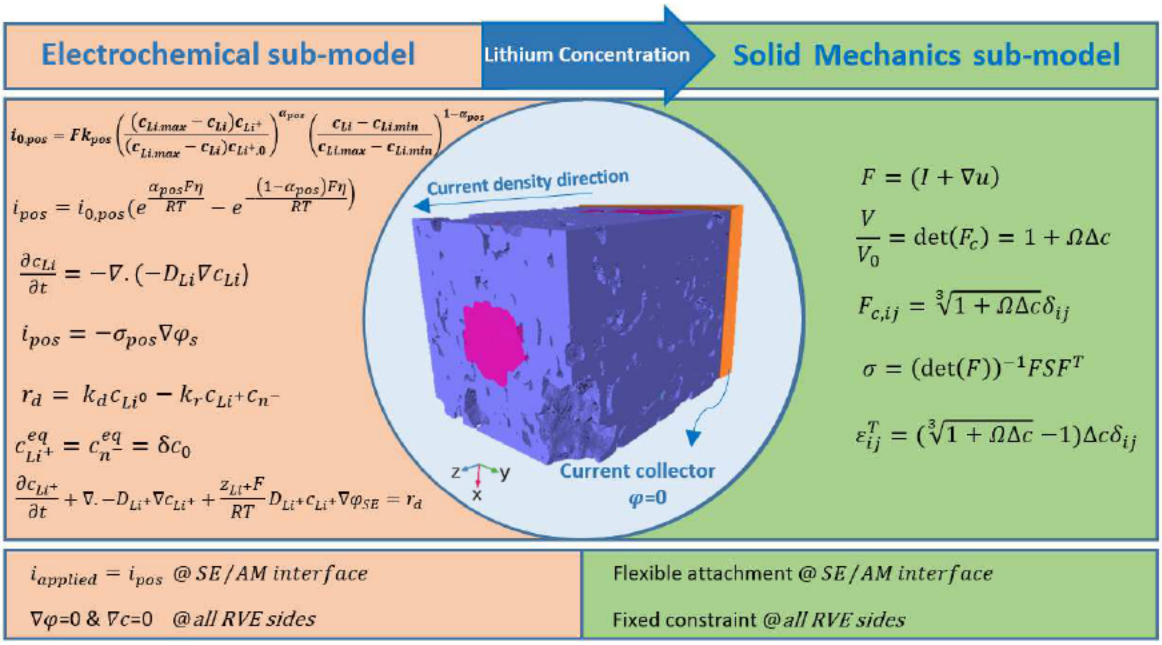

Figure 2 Modeling methodology including electrochemical and solid mechanics sub-models governing equations, boundary condition, current collector and current density direction.

Table 1 Model parameters

Parameter	Unit	Estimated Value	Description
$\boldsymbol{a_0}$	$mol\ m^{-3}$	6.01×10^4 [32]	Total activity of lithium atoms in SE matrix
$\boldsymbol{k_r}$	$m^3 mol^{-1} s^{-1}$	0.9×10^{-8} [32]	Lithium-ion recombination reaction rate
$\boldsymbol{\delta}$	-	0.18 [32]	Fraction of free lithium-ion in equilibrium
$\boldsymbol{D_{Li^+}}$	$m^2 s^{-1}$	0.9×10^{-13} [12]	Diffusion coefficient for lithium-ion in the SE (LTAP)
$\boldsymbol{D_{Li}}$	$m^2 s^{-1}$	1.76×10^{-13} [12]	Diffusion coefficient for lithium in AM (NMC)
$\boldsymbol{D_{n^-}}$	$m^2 s^{-1}$	5.1×10^{-13} [12]	Diffusion coefficient for n^- in the electrolyte
$\boldsymbol{a_{pos}^{max}}$	$mol\ m^{-3}$	2.33×10^4 [32]	Maximum activity of the lithium in the positive electrode
$\boldsymbol{\alpha_{pos}}$	-	0.6 [32]	Charge transfer coefficient in the positive electrode
$\boldsymbol{k_{poa}}$	$mol\ m^{-2} s^{-1}$	5.1×10^{-6} [32]	Rate constant charge transfer positive electrode
$\boldsymbol{\Omega}$	$m^3 mol^{-1}$	3×10^{-6} [4]	partial molar volume change of NMC-111
$\boldsymbol{E_{AM}}$	Gpa	199 [33]	Young's modulus of NMC-111
$\boldsymbol{v_{AM}}$	-	0.25 [33]	Poisson's ratio of NMC-111
$\boldsymbol{E_{SE}}$	Gpa	143.7 [34]	Young's modulus of LTAP
$\boldsymbol{v_{AM}}$	-	0.25 [34]	Poisson's ratio of LTAP

As mentioned, the reconstructed morphology was used to compute the electrochemical and solid mechanics equations. It is worth noting that utilizing the whole electrode microstructure can be computationally expensive. Therefore, a representative volume element (RVE) was chosen instead of the whole electrode microstructure. To ensure the validity of results in RVE, the SE, AM, and pore volume fractions and volume specific surface area of the AM were measured and compared at various RVE sizes to minimize the difference with the whole electrode structure. Therefore, the electrochemical and solid mechanics simulations were modeled on a sub-volume geometry with a dimension of $350 \times 350 \times 450$ Voxels (10867 μm^3) which has similar properties compared to the whole microstructure (**Table 2**) with less than 2% error.

Table 2 Volume specific surface area, AM, SE, and pore volume fractions in different RVE sizes in two composite electrodes with different external pressing pressures.

Pressing pressure 1300 psi							
Total Volume (μm^3)	19714	15968	12617	10867	7097	4929	3154
Volume specific surface area (1/μm)	0.601	0.614	0.620	0.621	0.635	0.649	0.658
Solid Active material (%)	28.5	28.2	27.9	28.8	27.5	27.1	24.3
Solid Electrolyte (%)	51.8	52.4	52.9	52.5	53.4	54.8	56.8
Pore (%)	19.7	19.4	19.2	18.7	19.1	18.1	18.9
Pressing pressure 700 psi							
Total Volume (μm^3)	19714	15968	12617	10867	7097	4929	3154
Volume specific surface area (1/μm)	0.502	0.514	0.522	0.521	0.538	0.551	0.567
Solid Active material (%)	29.3	28.7	28.3	29.9	27.4	26.1	25.4
Solid Electrolyte (%)	43.8	44.2	43.7	42.6	45.2	54.1	56.8
Pore (%)	26.9	27.1	28.0	27.5	27.4	19.8	17.8

4. Results and Discussion

The heterogeneous microstructure of the ASSB composite electrodes causes an in-homogenous distribution of physical and electrochemical properties within the electrodes' morphology. Additionally, the mechanical stability of the electrode highly relies on the microstructural design, and lithiation/delithiation induced expansion/contraction can cause contact loss and crack formation at the SE/AM interface [35]. To quantify the effect of the electrode morphology on the lithium distribution in the AM, the electrochemical sub-model methodology was implemented on the reconstructed microstructures fabricated under two external pressing pressures. During lithiation, there is a declining trend of lithium concentration in the AM along with the applied current density direction and a gradient in the AM particle radius direction due to lithium transport limitation. Moreover, at the surface of the AM particles, the imperfect SE/AM interface limits the Li-ion pathways, which causes a variation in lithium concentration. Increasing the external pressing pressure can enhance the contact area and lithium transport, which can be verified by a higher average of lithium concentration in the AM particles at any state of charge (SOC) for the electrode with 1300 psi external pressing pressure applied compared with 700 psi applied (***Figure A1***). To ensure the fidelity of results, the developed electrochemical model was validated and compared with the experimental data[12]. To highlight the heterogeneous distribution of lithiation induced stress within the composite electrode, the results are illustrated on either two cross-section planes (yz-xz) or the yz plane. **Figure *3*** presents the morphology of the electrodes fabricated with 1300 psi and 700 psi pressing pressure. It is worth noting that the ceramic SEs have a relatively good ionic conductivity; however, the main challenge is their hard and brittle nature [36]. Thus, mechanical incompatibility at the SE/AM interface may cause crack formation and performance degradation.

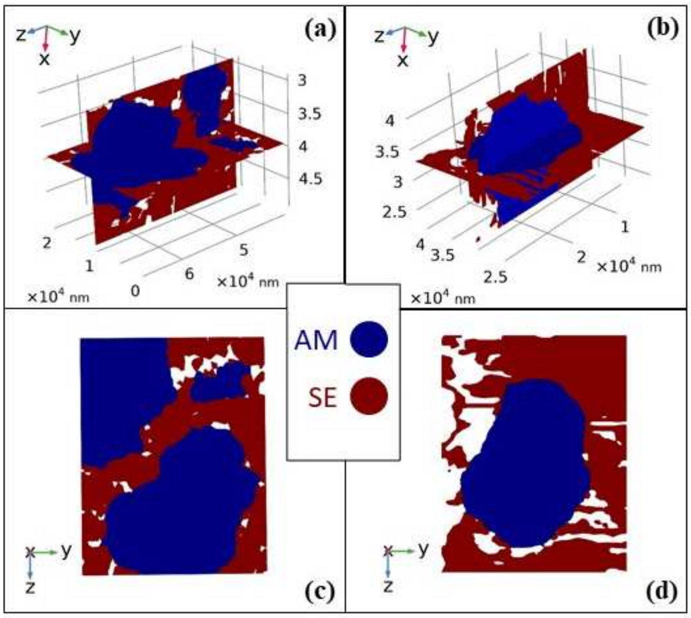

Figure 3 Cross-section view of the composite electrode with 1300 psi external pressing pressure in (a) two yz and xz planes, and (c) yz plane. Cross-section view of the composite electrode with 700 psi external pressing pressure in (b) two yz and xz planes, and (d) yz plane.

4.1. Effects of external pressing pressure

It is worth noting that although increasing the external pressing pressure can alleviate the SE/AM contact resistances and enhance the ion transport, it may negatively affect the mechanical stability of the electrode. The main reason for this is that lithium diffusion-induced volume change in AM particles can lead to crack formation and a loss of contact due to the excessive stress evolution at the interface. The lithiation-induced stress during the 1 C discharge rate in the composite electrode with 1300 psi external pressing pressure is illustrated in **Figure *4a-c*** using two cross-section planes. The maximum stress is observed at the end of lithiation due to high lithium concentration. With closer examination, anisotropic stress distribution within the AM particles not only depends on their shapes, but also depends on the void space distribution at the SE/AM interface. In other words, void spaces at the SE/AM interface could partially accommodate volume changes, and the AM particles undergo lower stress compared to points with perfect contact with the SE. To clarify the effect of the SE/AM interface on the stress distribution, the stress evolution over 1 C discharge in the composite electrode with 700 psi external pressing pressure is illustrated in **Figure *4d-f***. Comparing **Figure *4c*** and **Figure *4f***, it can be concluded that the electrode with lower external pressing pressure encounters low hydrostatic stress under the same operating conditions due to its lower SE/AM surface area. On the z-y plane, the hydrostatic stress at the AM/pore interface is as low as 0.7 GPa (end of discharge), while the hydrostatic stress at the SE/AM is within the range of 3-4 GPa at the same SOC. Throughout lithiation, the distribution of lithiation-induced stress within the AM follows the same trend while hydrostatic stress in AM particles is mostly compressive except near void spaces (***Figure* 4g-*l***).

To further elaborate on the effects of the external pressing pressure and the composite electrode microstructure on the distribution of lithiation-induced stress, the von Mises stress distribution is illustrated in **Figure *5***. The von Mises stress evolution in the composite electrode under 1300 psi pressing pressure during 1 C lithiation is presented in **Figure 5a-c** on two cross-section planes (defined in **Figure 3**) and **Figure 5g-i** on a yz plane. Under the same conditions, the Von Mises stress evolution for the electrode fabricated with 700 psi external pressing pressure is presented in **Figure 5d-f** for the two cross-section planes and yz plane (**Figure 5j-l**). The results show that the local maximum of von Mises stress occur at the SE/AM interface. For instance, at the end of lithiation, the composite electrode encounters several peak points of 5 Gpa at SE/AM interface while the von Mises stress at AM/pore interface is below 1 Gpa. Moreover, the electrode with higher pressing pressure has a relatively higher von Mises stress specifically at the SE/AM interface which could cause fracture formation within the SE. Although higher pressing pressure can enhance ion pathways and alleviate contact resistances at the SE/AM interface[12], it causes excessive stress evolution at the SE/AM interface. Therefore, the microstructural design of ASSBs is highly critical to find an optimal tradeoff of the fabrication process, such as external pressing pressure and the electrode chemo-mechanical performance.

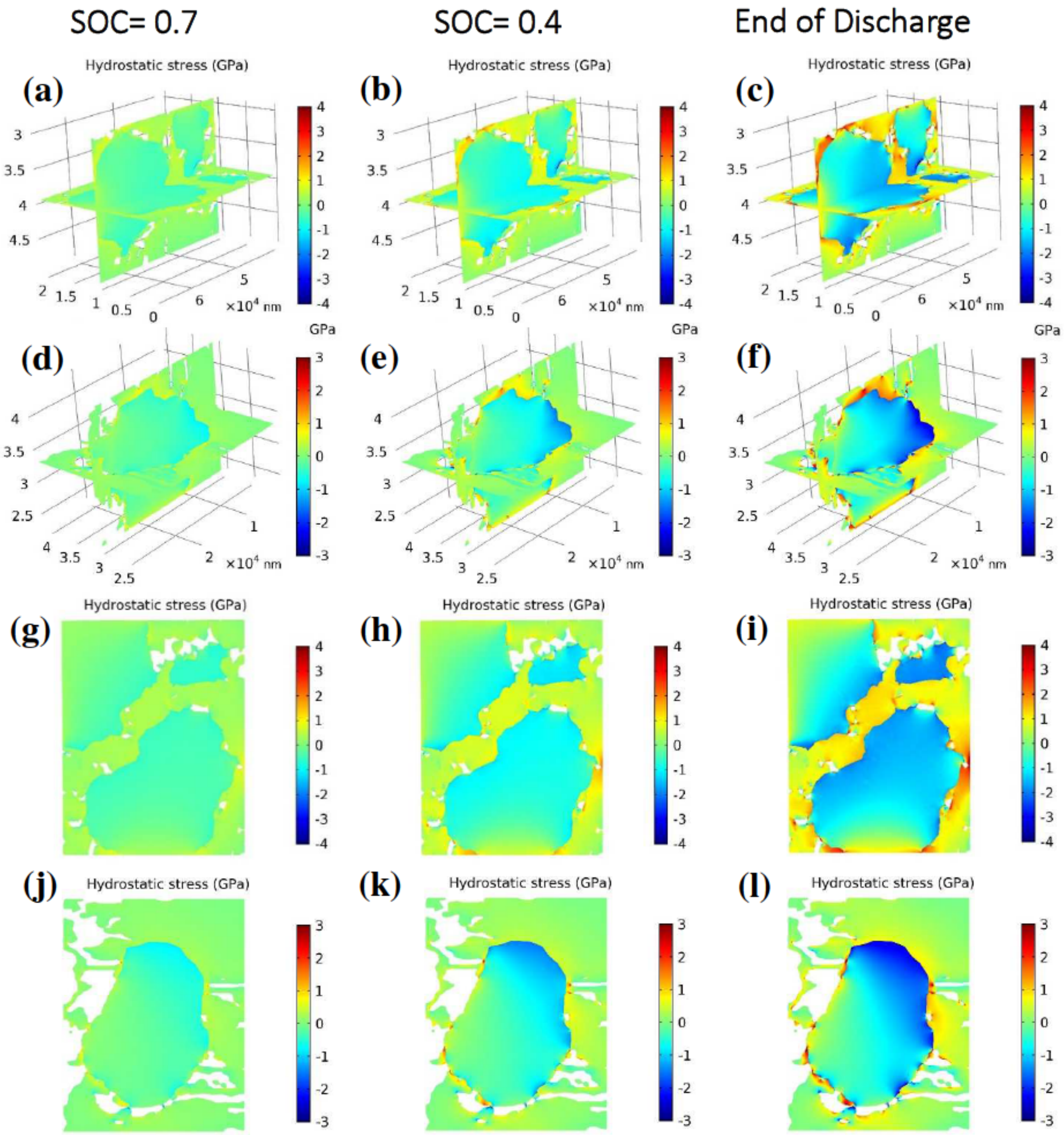

Figure 4 Hydrostatic stress in the composite electrode during 1C lithiation fabricated under (a-c) 1300 psi and (d-f) 700 psi illustrated in two cross-section planes (zy and xz). Hydrostatic stress in the composite electrode during 1C lithiation fabricated under (g-i) 1300 psi and (j-l) 700 Psi illustrated in yz plane.

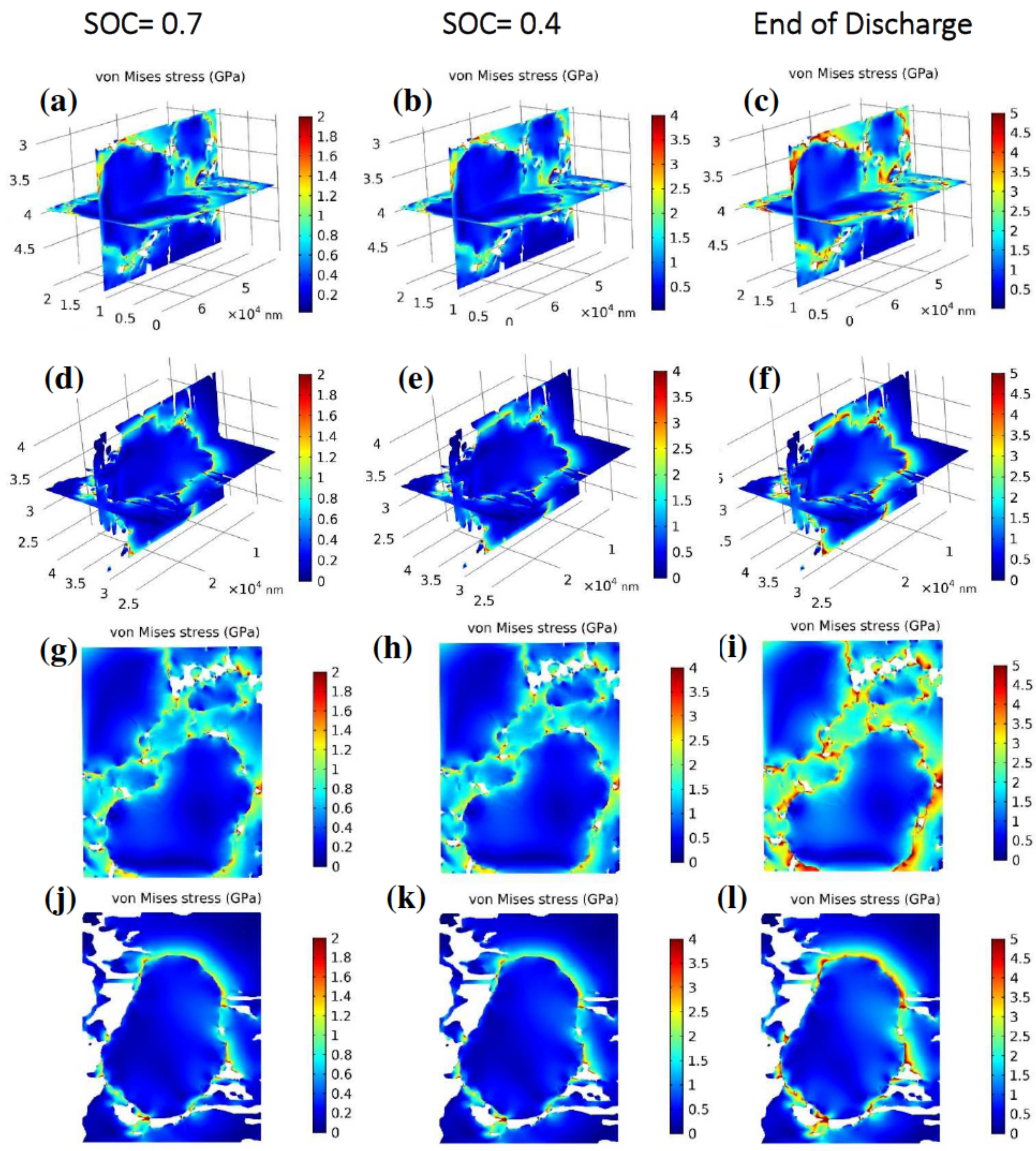

Figure 5 Von Mises stress in the composite electrode during 1C lithiation fabricated under (a-c) 1300 psi and (d-f) 700 psi illustrated in two cross-section planes (zy and xz). Von Mises stress in the composite electrode during 1C lithiation fabricated under

4.2. Effects of Current

In addition to morphological properties, applied current can affect the mechanical and electrochemical behavior of ASSBs. With increasing current, there is not enough time to fully lithiate the AMs, therefore the heterogeneous distribution of lithium concentration within the AM would have a wide range which limits the electrode capacity. The effects of current on electrochemical properties within the ASSB microstructure were previously investigated thoroughly[12]. On the other hand, applied current can attribute to stress evolution during battery operation. The hydrostatic von Mises stress during 3 C lithiation is compared with 1 C lithiation. The hydrostatic and von Mises stress are presented in **Figure 6a-c** and **Figure 6d-f** for 3 C lithiation in two cross-section planes, respectively. **Figure 6g-l** illustrates the aforementioned stresses on a yz plane with the same order. Comparing ***Figure 6*** with **Figure *4*** and **Figure *5***, it can be concluded that the hydrostatic stress and von Mises stress within the microstructure under 1 C and 3 C lithiation have almost an identical distribution. At high currents, lithium concentration has a relatively larger gradient within the AM particles and the lower lithium concentration at the particles' core may alleviate the stress evolution. The same observation was previously reported for other active materials such as silicon[37]. However, the partial molar volume of NMC is much lower than silicon. Thus, increasing current cannot significantly decrease the stress evolution within the microstructure (***Figure 6***). During cycling, the cathode electrolyte interfacial (CEI) layer intensifies the interfacial resistance [38]. In fact, the cathode interface resistance has a significant increase during the first charge [35]. It is expected that lithiation-induced stress, specifically at the SE/AM, can lead to an unstable CEI and crack formation which can exacerbate the interfacial resistance and cell degradation. Due to the mechanical incompatibility of the SE and AM, the maximum lithiation-induced stress is still expected to happen at the SE/AM interface in the real operation of ASSBs. In other words, SE and AM mechanical properties are the dominant parameters that trigger stress/strain variation within the composite electrode microstructure.

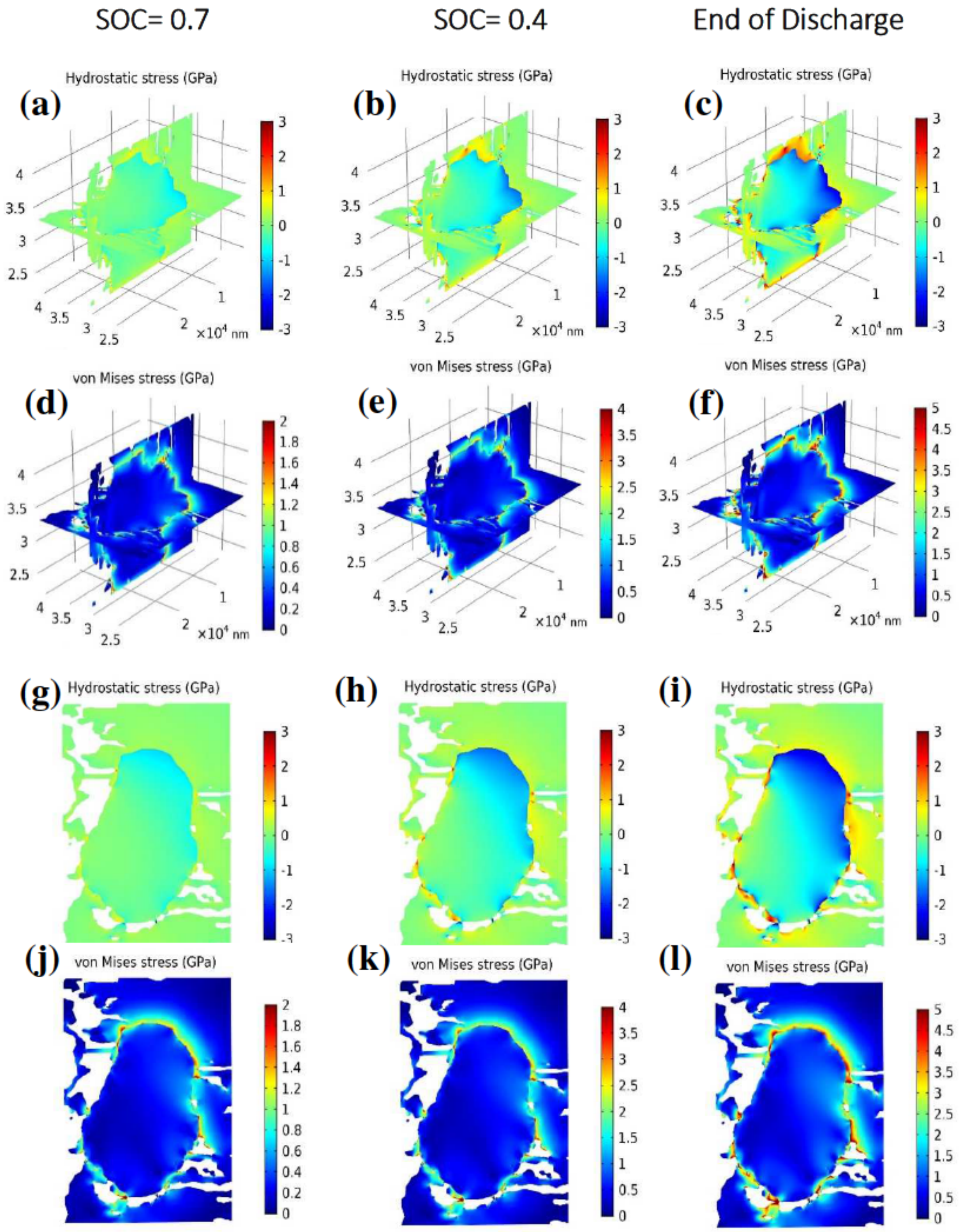

Figure 6 (a-c) Hydrostatic stress and (d-f) von Mises stress in the composite electrode during 3C lithiation fabricated 700 psi illustrated in two cross-section planes (zy and xz). (g-i) Hydrostatic stress and (j-i) von Mises stress in the composite electrode during 3C lithiation fabricated under 700 Psi illustrated in yz plane.

4.3. Effects of SE Stiffness

The mechanical properties of SEs have rarely been investigated in the literature, although optimizing the SE mechanical properties can effectively attenuate stress evolution within the composite electrode microstructure, and prevent fracture propagation and mechanical degradation. Although the Young's modulus of the SE in this study (LTAP) is 143.7 GPa, there is a wide range of available SEs with low stiffness, such as sulfide solid electrolytes that fall in the range of 14-25 GPa[11]. Overall, stiff SEs are more likely to undergo mechanical fracture and lose contact [39]. Therefore, to quantify the effect of SE stiffness, the hydrostatic and von Mises stress in the composite electrode are compared at two SE Young's modulus, 14.3 GPa and 143 Gpa. **Figure 7a-c** and **Figure 7d-f** illustrate the hydrostatic and von Mises stress respectively within the composite microstructure at the end of 1C lithiation for the SE with 14.3 GPa Young's modulus. **Figure 7g-l** presents the aforementioned stresses on a yz plane with the same order. The presented results show that the SE stiffness tremendously affects the lithiation-induced stress within the ASSBs' microstructure. For instance, at the end of lithiation, the maximum hydrostatic stress and von Mises stress in the composite electrode with the stiffer SE, are 3 GPa and 4.9 GPa, respectively; while in the other electrode (E_{SE}= 14.3 GPa), the maximum hydrostatic stress and von Mises stress are 0.6 GPa and 1 GPa, respectively. Thus, employing SE with low stiffness can be beneficial to inhibit stress evolution; however, the stiff electrolyte can suppress AM volume change. Suppressing AM expansion mostly becomes critical for alloy-based anode active materials which have relatively larger volume expansion, and to prevent dendrite formation on lithium metal anodes [40]. Therefore, optimizing the SE stiffness based on the application and AMs can balance the stress evolution and volume changes.

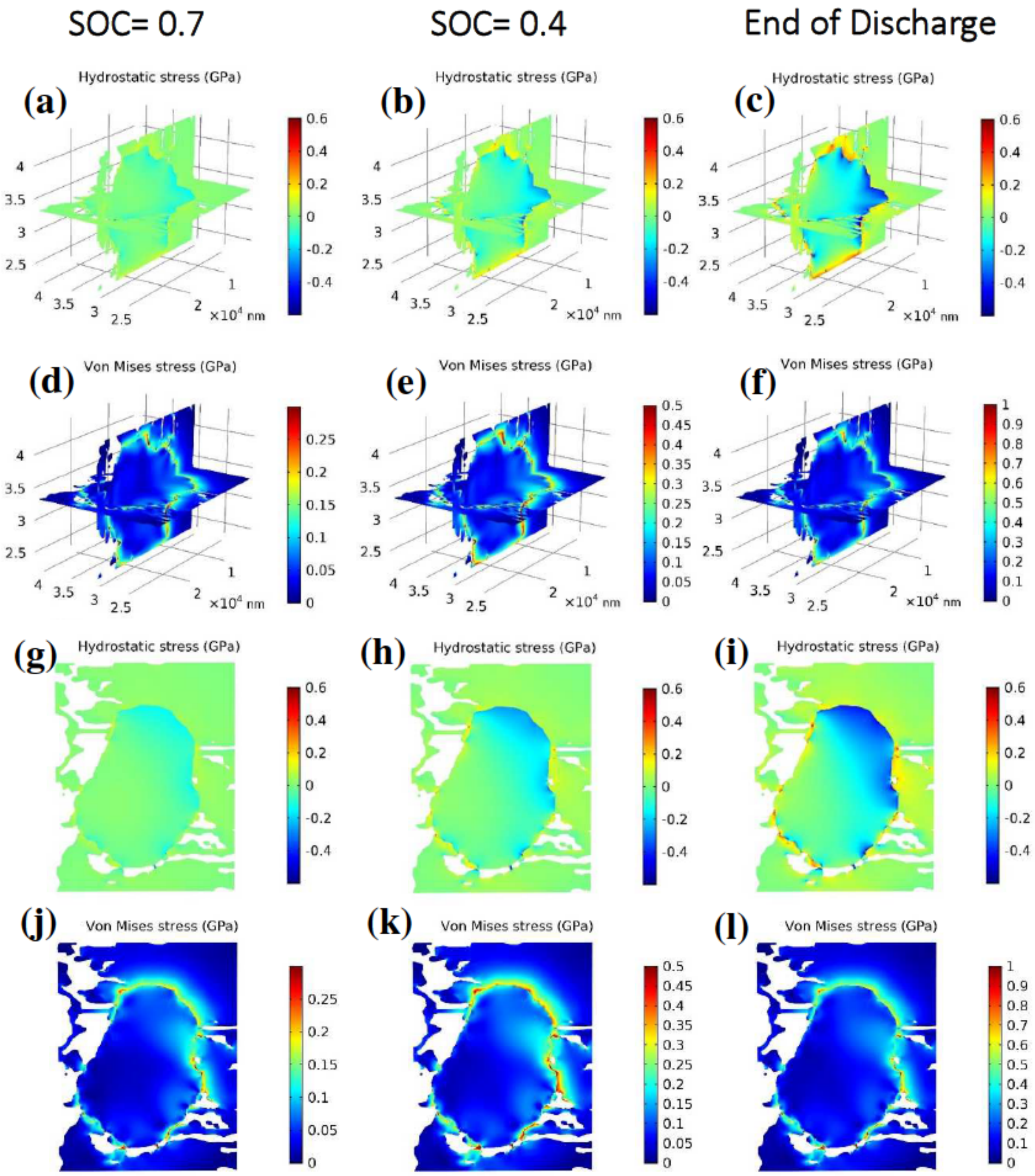

Figure 7 (a-c) Hydrostatic stress and (d-f) von Mises stress in the composite electrode during 1C lithiation fabricated under 700 psi external pressing pressure illustrated in two cross-section planes (zy and xz). (g-i) Hydrostatic stress and (j-i) von Mises stress in the composite electrode during 1C lithiation fabricated under 700 Psi illustrated in yz plane. SE Young's module is assumed to be 14.3 Gpa.

4.4. Anisotropic Displacement

Anisotropic volume changes of AM particles lead to a change in particle shape, which may cause mechanical degradation and contact loss with the SE [41]. The variation of directional displacement under 1 C lithiation in the AM phase of composite electrodes with 700 psi and 1300 psi external pressing pressure is illustrated in ***Figure 8a***. Displacement in the z-direction (parallel to the applied external pressing pressure) has the lowest value; while in the 700 psi electrode, the AM phase has a maximum displacement of 958 nm and 847 nm in the x- and y-directions (perpendicular to the applied external pressing pressure), respectively. With increased external pressing pressure, the displacement variation significantly decreased, where the AM phase maximum displacement becomes 439 nm and 259 nm in the x- and y-directions, respectively. The main reason is that external pressing pressure suppresses the void space and thus limits the displacement. Moreover, applying external pressing pressure can prevent anisotropic swelling of the active materials while directional displacement at lower external pressing pressure has a wider range of distribution (***Figure 8a***).

As mentioned in section 4.2, the current has a negligible effect on the lithiation-induced stress evolution within the electrode microstructure due to the relatively low partial molar volume expansion of the NMC. To further elaborate on this issue, the directional displacement of the AM phase under 1 C and 3 C lithiation are compared in ***Figure 8b***. The directional displacements, specifically at the perpendicular directions, are somewhat lower. At high currents, a larger gradient of lithium concentration within the AM particles causes slightly lower lithiation-induced expansion at the end of lithiation because the concentration at the AM particle surface reaches the cut-off value while the lithium concentration inside the particle is lower. Additionally, the effects of SE stiffness on the anisotropic displacement of the AM phase are illustrated in ***Figure 8c***. Although decreasing the SE Young's modulus can alleviate the stress evolution, the AM phase possesses relatively larger displacement which can intensify crack propagation within the microstructure. For instance, when changing the SE Young's modulus from 143.7 GPa to 14.3 GPa, the AM maximum displacement at the end of lithiation is 2350 nm and 2300 nm in the x- and y-direction, respectively.

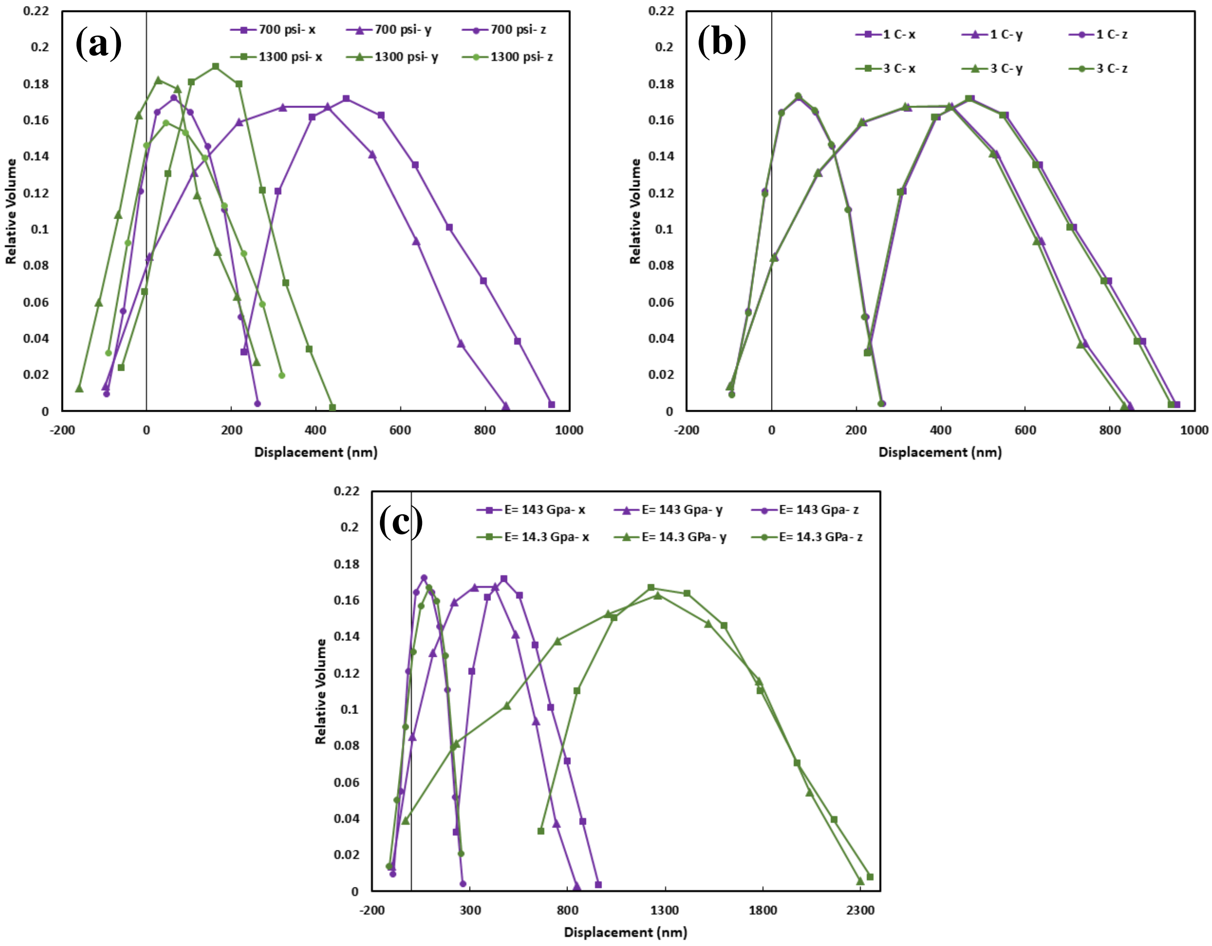

Figure 3 (a) Directional displacement of AM phase in composite electrodes with 700 psi and 1300 psi external pressing pressure during 1C lithiation and (b) directional displacement of AM phase phase in composite electrodes with 700 psi external pressing pressure during 1C and 3C lithiation

5. Conclusion

In this study, we developed a chemo-mechanical model for ASSBs composite electrode that incorporates a 3D reconstructed microstructure of the electrode using TXM images, fabricated under two external pressing pressures. The simulation results revealed the effects of the SE/AM interface and void space distribution within the microstructure on the lithiation-induced stress during the battery operation. The results show that AM particles encounter compressive hydrostatic stress up to 4 GPa at the SE/AM interface during lithiation, while the SE limits their expansion. On the other hand, void space can partially accommodate the AM expansion, where areas near void spaces have tensile stress within the range of 0-1 Gpa. The electrode with higher external pressing pressure experiences a relatively higher hydrostatic stress due to a higher SE/AM interfacial contact and the decreased amount of void space. The simulated von Mises stress confirms this behavior. At the end of lithiation, the von Mises stress in AM particles is approximately zero while at the surface, the AM contains up to 4.9 GPa stress which could cause crack formation and mechanical degradation. The electrode with higher pressing pressure has more peak stress points and the average von Mises stress within the microstructure with higher pressing pressure is 2.4 GPa compared to 1.5 GPa with lower pressing pressure. Therefore, the microstructural design of the SE/AM interface is critical to find an optimal tradeoff of maximizing ion pathways and minimizing the stress evolution. It was also shown that unlike anode AMs, which have larger volume expansion, the effects of current on the stress evolution in the composite cathode microstructure is negligible due to the relatively small partial molar volume of cathode AMs. However, SE stiffness has a significant impact on the stress evolution and anisotropic displacement in the composite electrode. Decreasing SE stiffness, can adjust the maximum hydrostatic and von Mises stress from 3 GPa and 4.9 GPa to 0.6 GPa and 1 GPa, respectively. Conversely, the stiff SE can suppress AM swelling and attenuate anisotropic displacement of AMs which may improve the mechanical integrity of the composite electrode.

Acknowledgments

The authors thank Tyler Or for the review of the manuscript. CMC Microsystems is acknowledged for the provision of products and services that facilitated this research, including COMSOL Multiphysics and providing computational facilities. This work was supported by the US National Science Foundation under Grant 1335850 and used resources of the Advanced Photon Source, a U.S. Department of Energy (DOE) Office of Science User Facility operated for the DOE Office of Science by Argonne National Laboratory under Contract DE-AC02-06CH11357. This research was also supported by the Natural Sciences and Engineering Research Council of Canada (NSERC) through grants to Z.C. and the University of Waterloo.

Appendix A

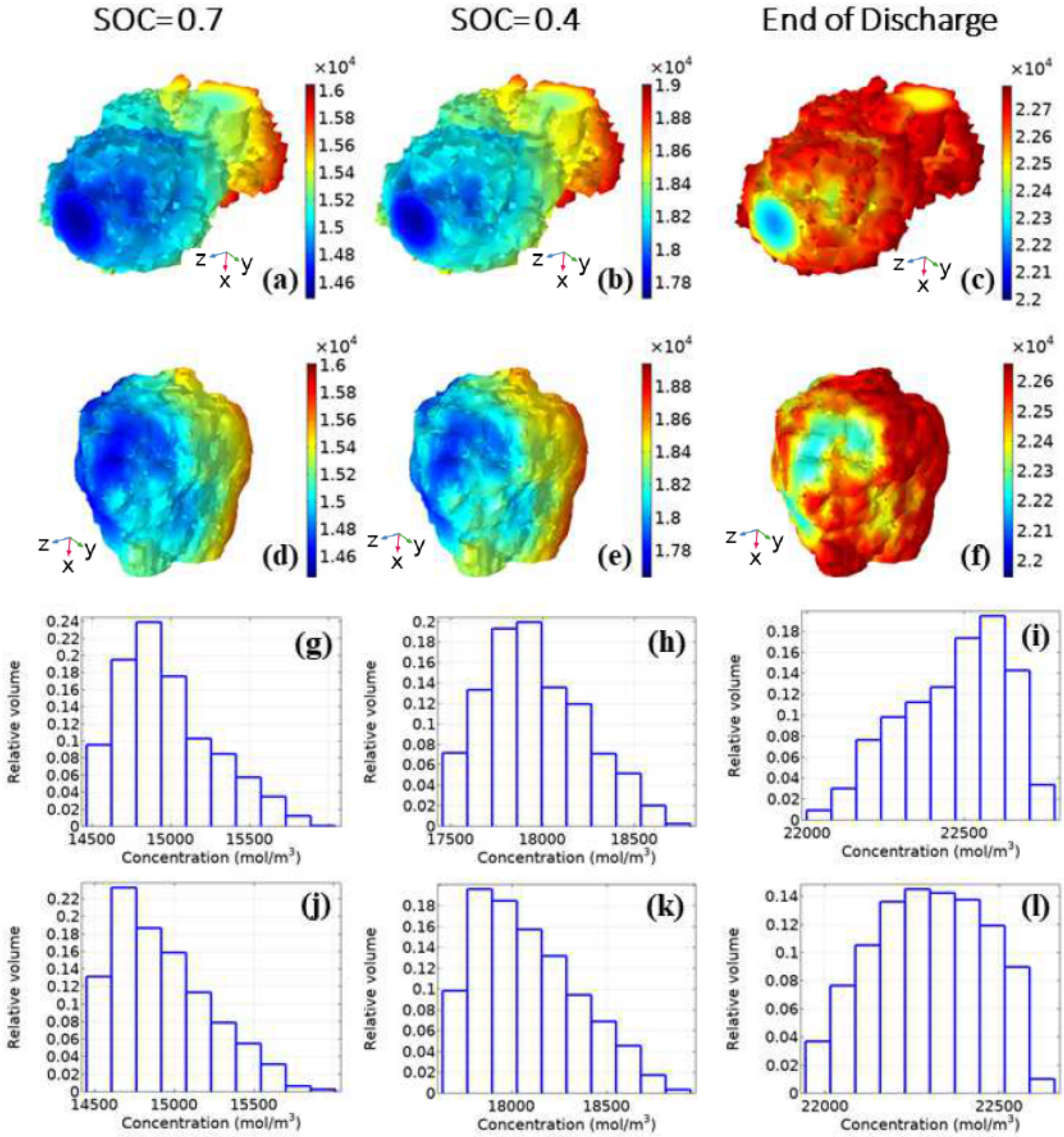

Figure A1 Lithium concentration in AM under two external pressing pressure (a-c) 1300 psi and (d-f) 700 psi during 3.2 C discharge rate. Histograms illustrate the lithium concentration in AM under two external pressing pressure (g-i) 1300 psi and (j-l) 700 psi during 3.2 C discharge rate.

Supplementary Video.mp4

Supplementary video Lithium concentration, von Mises stress, and hydrostatic stress in AM phase of composite ASSB's electrode fabricated under 700 psi external pressing pressure during 1 C lithiation

References

1. Gandoman, F. H.; Jaguemont, J.; Goutam, S.; Gopalakrishnan, R.; Firouz, Y.; Kalogiannis, T.; Omar, N.; Van Mierlo, J. J. A. E., Concept of reliability and safety assessment of lithium-ion batteries in electric vehicles: Basics, progress, and challenges. **2019,** *251*, 113343.
2. Gao, Z.; Sun, H.; Fu, L.; Ye, F.; Zhang, Y.; Luo, W.; Huang, Y. J. A. m., Promises, challenges, and recent progress of inorganic solid-state electrolytes for all-solid-state lithium batteries. **2018,** *30* (17), 1705702.
3. Wang, P.; Qu, W.; Song, W. L.; Chen, H.; Chen, R.; Fang, D. J. A. F. M., Electro–Chemo–Mechanical Issues at the Interfaces in Solid-State Lithium Metal Batteries. **2019,** *29* (27), 1900950.
4. Koerver, R.; Zhang, W.; de Biasi, L.; Schweidler, S.; Kondrakov, A. O.; Kolling, S.; Brezesinski, T.; Hartmann, P.; Zeier, W. G.; Janek, J. J. E.; Science, E., Chemo-mechanical expansion of lithium electrode materials–on the route to mechanically optimized all-solid-state batteries. **2018,** *11* (8), 2142-2158.
5. Zhang, Y.; Zhao, C.; Guo, Z. J. I. J. o. M. S., Simulation of crack behavior of secondary particles in Li-ion battery electrodes during lithiation/de-lithiation cycles. **2019,** *155*, 178-186.
6. Bucci, G.; Talamini, B.; Balakrishna, A. R.; Chiang, Y.-M.; Carter, W. C. J. P. R. M., Mechanical instability of electrode-electrolyte interfaces in solid-state batteries. **2018,** *2* (10), 105407.
7. He, Y.; Lu, C.; Liu, S.; Zheng, W.; Luo, J. J. A. E. M., Interfacial Incompatibility and Internal Stresses in All-Solid-State Lithium Ion Batteries. **2019,** *9* (36), 1901810.
8. Li, T.; Kang, H.; Zhou, X.; Lim, C.; Yan, B.; De Andrade, V.; De Carlo, F.; Zhu, L. J. A. a. m.; interfaces, Three-Dimensional Reconstruction and Analysis of All-Solid Li-Ion Battery Electrode Using Synchrotron Transmission X-ray Microscopy Tomography. **2018,** *10* (20), 16927-16931.
9. Sethuraman, V. A.; Chon, M. J.; Shimshak, M.; Srinivasan, V.; Guduru, P. R. J. J. o. P. S., In situ measurements of stress evolution in silicon thin films during electrochemical lithiation and delithiation. **2010,** *195* (15), 5062-5066.
10. Pharr, M.; Suo, Z.; Vlassak, J. J. J. N. l., Measurements of the fracture energy of lithiated silicon electrodes of Li-ion batteries. **2013,** *13* (11), 5570-5577.
11. Bucci, G.; Swamy, T.; Chiang, Y.-M.; Carter, W. C. J. J. o. M. C. A., Modeling of internal mechanical failure of all-solid-state batteries during electrochemical cycling, and implications for battery design. **2017,** *5* (36), 19422-19430.
12. Fathiannasab, H.; Kashkooli, A. G.; Li, T.; Zhu, L.; Chen, Z. J. J. o. t. E. S., Three-Dimensional Modeling of All-Solid-State Lithium-Ion Batteries Using Synchrotron Transmission X-ray Microscopy Tomography. **2020**.
13. Nolan, A. M.; Zhu, Y.; He, X.; Bai, Q.; Mo, Y. J. J., Computation-accelerated design of materials and interfaces for all-solid-state lithium-ion batteries. **2018,** *2* (10), 2016-2046.
14. Tian, H.-K.; Chakraborty, A.; Talin, A. A.; Eisenlohr, P.; Qi, Y. J. J. o. T. E. S., Evaluation of The Electrochemo-Mechanically Induced Stress in All-Solid-State Li-Ion Batteries. **2020,** *167* (9), 090541.
15. Song, X.; Lu, Y.; Wang, F.; Zhao, X.; Chen, H. J. J. o. P. S., A coupled electro-chemo-mechanical model for all-solid-state thin film Li-ion batteries: The effects of bending on battery performances. **2020,** *452*, 227803.
16. Yu, H.-C.; Taha, D.; Thompson, T.; Taylor, N. J.; Drews, A.; Sakamoto, J.; Thornton, K. J. J. o. P. S., Deformation and stresses in solid-state composite battery cathodes. **2019,** *440*, 227116.
17. Kashkooli, A. G.; Farhad, S.; Lee, D. U.; Feng, K.; Litster, S.; Babu, S. K.; Zhu, L.; Chen, Z. J. J. o. P. S., Multiscale modeling of lithium-ion battery electrodes based on nano-scale X-ray computed tomography. **2016,** *307*, 496-509.

18. Kashkooli, A. G.; Foreman, E.; Farhad, S.; Lee, D. U.; Ahn, W.; Feng, K.; De Andrade, V.; Chen, Z. J. E. A., Synchrotron X-ray nano computed tomography based simulation of stress evolution in LiMn2O4 electrodes. **2017,** *247*, 1103-1116.

19. Choi, S.; Jeon, M.; Ahn, J.; Jung, W. D.; Choi, S. M.; Kim, J.-S.; Lim, J.; Jang, Y.-J.; Jung, H.-G.; Lee, J.-H. J. A. a. m.; interfaces, Quantitative analysis of microstructures and reaction interfaces on composite cathodes in all-solid-state batteries using a three-dimensional reconstruction technique. **2018,** *10* (28), 23740-23747.

20. Tippens, J.; Miers, J. C.; Afshar, A.; Lewis, J. A.; Cortes, F. J. Q.; Qiao, H.; Marchese, T. S.; Di Leo, C. V.; Saldana, C.; McDowell, M. T. J. A. E. L., Visualizing chemomechanical degradation of a solid-state battery electrolyte. **2019,** *4* (6), 1475-1483.

21. Choi, S.; Yun, B.-N.; Jung, W. D.; Kim, T. H.; Chung, K.-Y.; Son, J.-W.; Sang, B.-I.; Jung, H.-G.; Kim, H. J. S. M., Tomographical analysis of electrochemical lithiation and delithiation of LiNi0. 6Co0. 2Mn0. 2O2 cathodes in all-solid-state batteries. **2019,** *165*, 10-14.

22. Ohashi, A.; Kodama, M.; Xueying, S.; Hori, S.; Suzuki, K.; Kanno, R.; Hirai, S. J. J. o. P. S., Stress distribution in the composite electrodes of sulfide all-solid-state lithium-ion batteries. **2020,** *470*, 228437.

23. Li, T.; Kang, H.; Zhou, X.; Lim, C.; Yan, B.; De Andrade, V.; De Carlo, F.; Zhu, L. J. A. a. m.; interfaces, Three-Dimensional Reconstruction and Analysis of All-Solid Li-Ion Battery Electrode Using Synchrotron Transmission X-ray Microscopy Tomography. **2018**.

24. Asl, N. M.; Keith, J.; Lim, C.; Zhu, L.; Kim, Y. J. E. a., Inorganic solid/organic liquid hybrid electrolyte for use in Li-ion battery. **2012,** *79*, 8-16.

25. Wolff, N.; Roeder, F.; Krewer, U. J. E. A., Model based assessment of performance of lithium-ion batteries using single ion conducting electrolytes. **2018,** *284*, 639-646.

26. Kazemi, N.; Danilov, D. L.; Haverkate, L.; Dudney, N. J.; Unnikrishnan, S.; Notten, P. H. J. S. S. I., Modeling of all-solid-state thin-film Li-ion batteries: Accuracy improvement. **2019,** *334*, 111-116.

27. Raijmakers, L.; Danilov, D.; Eichel, R.-A.; Notten, P. J. E. A., An advanced all-solid-state Li-ion battery model. **2020,** *330*, 135147.

28. Danilov, D.; Niessen, R.; Notten, P. J. J. o. t. E. S., Modeling all-solid-state Li-ion batteries. **2010,** *158* (3), A215.

29. Wang, M.; Xiao, X. J. J. o. P. S., Investigation of the chemo-mechanical coupling in lithiation/delithiation of amorphous Si through simulations of Si thin films and Si nanospheres. **2016,** *326*, 365-376.

30. Wang, M.; Xiao, X.; Huang, X. J. J. o. P. S., A multiphysics microstructure-resolved model for silicon anode lithium-ion batteries. **2017,** *348*, 66-79.

31. Wang, M.; Xiao, X.; Huang, X. J. J. o. P. S., Study of lithium diffusivity in amorphous silicon via finite element analysis. **2016,** *307*, 77-85.

32. Danilov, D.; Niessen, R.; Notten, P. J. J. o. t. E. S., Modeling all-solid-state Li-ion batteries. **2011,** *158* (3), A215-A222.

33. Cheng, E. J.; Hong, K.; Taylor, N. J.; Choe, H.; Wolfenstine, J.; Sakamoto, J. J. J. o. t. E. C. S., Mechanical and physical properties of LiNi0. 33Mn0. 33Co0. 33O2 (NMC). **2017,** *37* (9), 3213-3217.

34. Deng, Z.; Wang, Z.; Chu, I.-H.; Luo, J.; Ong, S. P. J. J. o. T. E. S., Elastic properties of alkali superionic conductor electrolytes from first principles calculations. **2015,** *163* (2), A67.

35. Koerver, R.; Aygün, I.; Leichtweiß, T.; Dietrich, C.; Zhang, W.; Binder, J. O.; Hartmann, P.; Zeier, W. G.; Janek, J. r. J. C. o. M., Capacity fade in solid-state batteries: interphase formation and chemomechanical processes in nickel-rich layered oxide cathodes and lithium thiophosphate solid electrolytes. **2017,** *29* (13), 5574-5582.

36. Lim, Y. J.; Kim, H. W.; Lee, S. S.; Kim, H. J.; Kim, J.-K.; Jung, Y.-G.; Kim, Y. J. C., Ceramic-based composite solid electrolyte for lithium-ion batteries. **2015,** *80* (7), 1100.

37. Gao, X.; Lu, W.; Xu, J. J. J. o. P. S., Modeling framework for multiphysics-multiscale behavior of Si–C composite anode. **2020,** *449*, 227501.

38. Wang, Z.; Lee, J. Z.; Xin, H. L.; Han, L.; Grillon, N.; Guy-Bouyssou, D.; Bouyssou, E.; Proust, M.; Meng, Y. S. J. J. o. P. S., Effects of cathode electrolyte interfacial (CEI) layer on long term cycling of all-solid-state thin-film batteries. **2016,** *324*, 342-348.

39. Pervez, S. A.; Cambaz, M. A.; Thangadurai, V.; Fichtner, M. J. A. a. m.; interfaces, Interface in solid-state lithium battery: challenges, progress, and outlook. **2019,** *11* (25), 22029-22050.

40. Zhang, F.; Huang, Q.-A.; Tang, Z.; Li, A.; Shao, Q.; Zhang, L.; Li, X.; Zhang, J. J. N. E., A review of mechanics-related material damages in all-solid-state batteries: Mechanisms, performance impacts and mitigation strategies. **2020,** *70*, 104545.

41. Wu, X.; Billaud, J.; Jerjen, I.; Marone, F.; Ishihara, Y.; Adachi, M.; Adachi, Y.; Villevieille, C.; Kato, Y. J. A. E. M., Operando Visualization of Morphological Dynamics in All-Solid-State Batteries. **2019,** *9* (34), 1901547.